

We are IntechOpen, the world's leading publisher of Open Access books Built by scientists, for scientists

6,900

Open access books available

186,000

International authors and editors

200M

Downloads

Our authors are among the

154

Countries delivered to

TOP 1%

most cited scientists

12.2%

Contributors from top 500 universities



WEB OF SCIENCE™

Selection of our books indexed in the Book Citation Index
in Web of Science™ Core Collection (BKCI)

Interested in publishing with us?
Contact book.department@intechopen.com

Numbers displayed above are based on latest data collected.
For more information visit www.intechopen.com



Plasmonic Nanopores: Optofluidic Separation of Nano-Bioparticles via Negative Depletion

*Xiangchao Zhu, Ahmet Cicek, Yixiang Li
and Ahmet Ali Yanik*

Abstract

In this chapter, we review a novel “optofluidic” nanopore device enabling label-free sorting of nano-bioparticles [e.g., exosomes, viruses] based-on size or chemical composition. By employing a broadband objective-free light focusing mechanism through extraordinary light transmission effect, our plasmonic nanopore device eliminates sophisticated instrumentation requirements for precise alignment of optical scattering and fluidic drag forces, a fundamental shortcoming of the conventional optical chromatography techniques. Using concurrent optical gradient and radial fluidic drag forces, it achieves self-collimation of nano-bioparticles with inherently minimized spatial dispersion against the fluidic flow. This scheme enables size-based fractionation through negative depletion and refractive-index based separation of nano-bioparticles from similar size particles that have different chemical composition. Most remarkably, its small ($4\ \mu\text{m} \times 4\ \mu\text{m}$) footprint facilitates on-chip, multiplexed, high-throughput nano-bioparticle sorting using low-cost incoherent light sources.

Keywords: plasmonic nanopore, optical tweezers, optofluidics, extraordinary light transmission, nano-bioparticle sorting

1. Introduction

Optical chromatography (OC) is an increasingly adapted technique for label-free sorting and analysis of bioparticles including cells, bacteria, fungi [1–4]. It exploits a lightly focused Gaussian laser beam within a microfluidic channel to create opposing optical scattering and fluidic drag forces. One can leverage these controllable forces to realize selective fractionation of bioparticles in a heterogeneous mixture based on size, morphology or chemical composition (i.e., refractive index variation) [5, 6]. OC technique was first implemented in size-based fractionation of inorganic materials such as polystyrene beads. Later, researchers employed this technique for size-based fractionation and sorting of organic particles including human blood constituents including erythrocytes, monocytes, granulocytes, and lymphocytes [2, 5]. Subsequently, differentiation of micronscale bioparticles with subtle differences [4, 7], including those with size differences as small as 70 nm [8], are shown. In addition to size-based separation, OC technique also offers refractive index-based fractionation capability, allowing separation of bioparticles with

minuscule differences in chemical composition, such as *Bacillus anthracis* and *Bacillus thuringiensis* [4] and cells with single gene modifications [3]. Most recently, precise separation capability of OC technique is utilized in realization of multi-stage fractionation approaches enabling network-based microfluidic purification [9, 10]. On the other hand, conventional OC technique suffers from powerful laser beam requirements to create sufficiently strong optical scattering forces [2], as well as multiple off-chip and bulky optical multi-axis positioners that are needed to realize well-controlled laser beam profiles precisely aligned against the fluidic flow [5]. Furthermore, separate sets of light sources and optical components are needed for each processing channels, preventing multiplexed high-throughput operation [10].

In a recent publication, we introduced a novel plasmonic nanopore device that eliminates the shortcomings of the conventional OC technique [11]. Here, we review this hybrid Optofluidic PlasmonIC (OPtIC) device merging light focusing and fluidic flow through a tiny ($4\ \mu\text{m} \times 4\ \mu\text{m}$ footprint) plasmonic microlens housing an integrated nanopore channel. Based on a subwavelength-thick ($\sim 200\ \text{nm}$) suspended device structure, our optofluidic approach opens the door to practical, scalable, and high-throughput on-chip particle sorting.

2. OPtIC microlens design

In **Figure 1a**, an OPtIC device that consists of a periodic nanohole array (NHA) defined in a suspended multilayer membrane is shown. The mechanically robust membrane consists of a free-standing 100 nm thick silicon nitride (Si_3N_4) substrate coated with 100 nm thick gold (Au) and a 5 nm thick titanium (Ti) adhesion layer. The total thickness of the microlens is $h = t_{\text{Au}} + t_{\text{Ti}} + t_{\text{Si}_3\text{N}_4} = 205\ \text{nm}$, whereas the lateral dimension of the finite size NHA is $4\ \mu\text{m} \times 4\ \mu\text{m}$. Recent research findings suggest that (quasi)periodic arrays of nanoplasmonic apertures behave as micro-convex lenses focusing broadband incoherent light beams to spot sizes comparable to wavelength of light [11–13]. Such tight light focusing capability can be harnessed to realize sufficiently strong optical scattering forces suitable for OC using collimated broadband light sources [14, 15]. In addition, the finite-size plasmonic NHAs can focus light over a broad wavelength range with focusing characteristics dictated by the lateral dimension of the array and nearly insensitive to sub-structural imperfections [13]. In this respect, our plasmonic nanopore device provides a distinct nanofluidic integration capability through small modifications in the NHA design without degrading its light focusing characteristics. The periodic NHA shown in **Figure 1a** consists of $d = 150\ \text{nm}$ diameter openings with a periodicity of $a = 380\ \text{nm}$. Enhanced light transmission through the periodic nanohole around this center nanoaperture occurs through the extraordinary optical transmission (EOT) effect [16–19]. The enlarged central nanopore with $d_c = 500\ \text{nm}$ exhibits orders of magnitude smaller fluidic resistance with respect to the neighboring nanoholes, enabling efficient nanofluidic flow through it. The OPtIC device uses inlet and outlet fluidic ports that are on the opposite sides of the NHA [20, 21], as depicted in **Figure 1b**. This design facilitates microfluidic access from either side of the membrane [22]. In our simulations, $50\ \mu\text{m}$ distance in between of the inlet and outlet fluidic ports is chosen to provide a clear path for the focused light beam [20].

Figure 1b depicts the cross-sectional view of nanofluidic flow pattern across the OPtIC device calculated using steady-state finite-element method (FEM) simulations (COMSOL Multiphysics). The overall size of the computational domain in **Figure 1b** is $50\ \mu\text{m} \times 50\ \mu\text{m} \times 40\ \mu\text{m}$. The inlet fluidic flow is directed towards the central aperture, where flow velocity is largest along the optical (z) axis in the vicinity of the optical focal point, whereas an almost symmetric behavior is

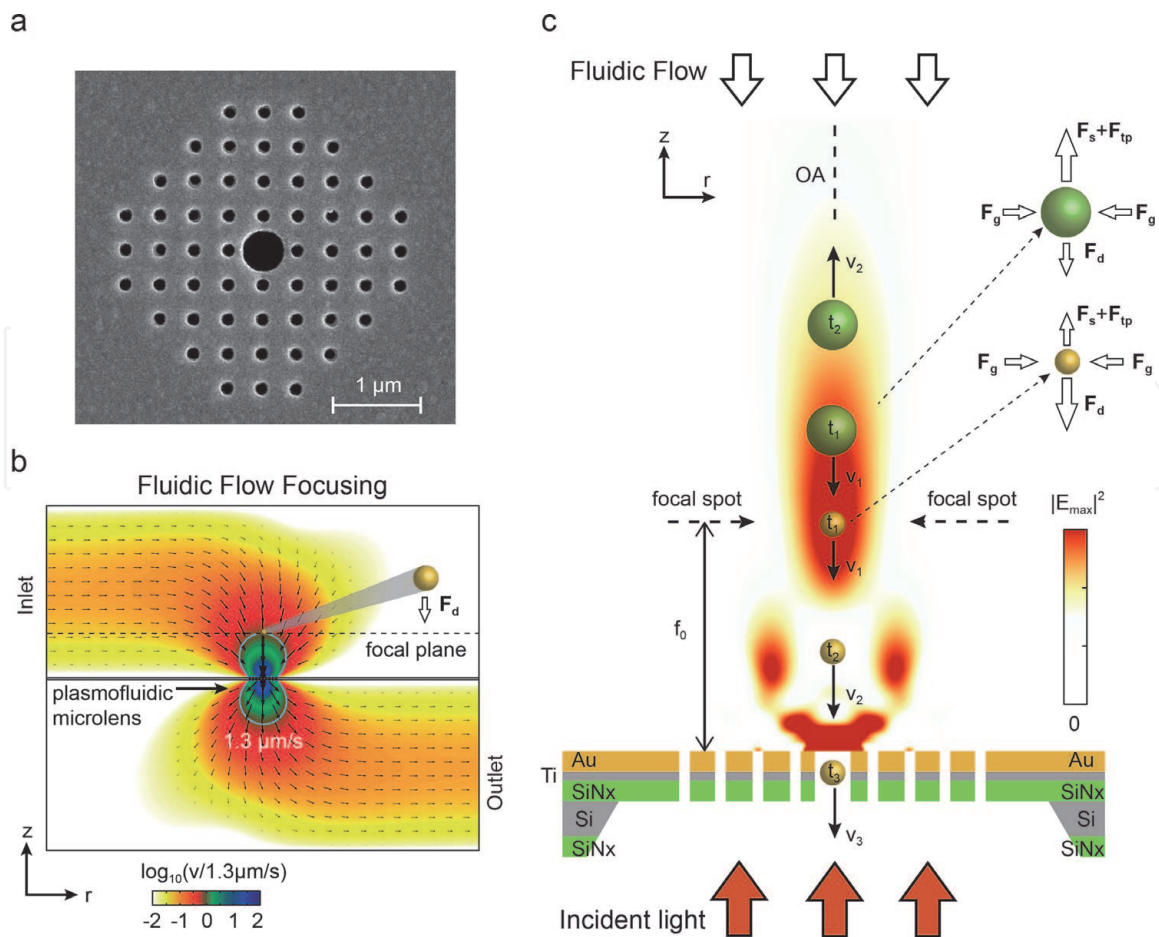


Figure 1. OPtIC nanopore device enabling selective sorting of bioparticles: (a) top view of OPtIC microlens consisting of a 9×9 NHA with enlarged central aperture. (b) Nanofluidic flow pattern across the OPtIC device with $1.3 \mu\text{m/s}$ flow rate at the focal point. (c) Conceptual illustration of the selective separation mechanism for nano-bioparticles through counter acting forces at the focal point. Copyright 2020 nature publishing group adapted with permission [11].

observed towards the outlet port. The observed fluidic flow pattern can be understood through the Hagen-Poiseille law, where the pressure-driven flow across a cylindrical aperture with hydraulic diameter r_H and thickness h occurs with a volumetric flow rate given by $Q = \Delta p/R_H$ (in m^3s^{-1}). Here, Δp is the pressure gradient across the aperture and $R_H = 8\mu h/\pi r_H^4$ (in $\text{Pa}\cdot\text{s}^3\text{m}^{-1}$ with $\mu = 8.9 \times 10^{-4} \text{Pa}\cdot\text{s}$ being dynamic viscosity of water) is the hydraulic resistance [23]. Since the hydraulic resistance is inversely proportional to the 4th power of hydraulic radius, it is two orders of magnitude smaller across the central aperture with respect to the rest of the holes in the NHA. Hence, convective fluidic flow, which follows the least resistance path, is through the central nanoaperture, as shown in our simulations. In summary, the OPtIC device forces nano-bioparticles to flow towards its focal point, where the dynamic flow trajectories of the particles are aligned with the optical axis of the plasmonic microlens.

A close-up cross-sectional view of the OPtIC device is given in **Figure 1c**, where the fluidic flow is in the $-z$ direction within the close vicinity of the focal point (f_0 away from microlens top) as explained above. In this configuration, the collimated light incident from bottom along the $+z$ direction is focused by the plasmonic microlens along the optical axis. Here, the focusing pattern, the amplitude-squared electric field ($\sim|E|^2$), is calculated through finite-difference time-domain (FDTD) simulations for incident light at $\lambda = 655 \text{ nm}$. Forces acting on two different sized nano-bioparticles within the focal point region are depicted on the right of the **Figure 1c**. Here, the optical scattering force (F_s) is inherently aligned against the

fluidic drag force (\mathbf{F}_d) along the optical axis for both particles. In addition, thermo-plasmonic drag force (\mathbf{F}_{tp}) caused by electromagnetic heating acts in parallel to \mathbf{F}_s . This will be explained in detail later. In addition to radial drag forces ($\mathbf{F}_{d,r}$) due to the fluidic flow, the optical gradient forces (\mathbf{F}_g) collimate particles along the optical axis, thus providing a robust mechanism for their precise alignment along the optical axis.

Figure 1c depicts that large particles with diameters above a threshold are driven against the fluid flow (i.e. in the $+z$ direction) provided that \mathbf{F}_s is sufficiently larger than \mathbf{F}_d . This is also true for particles with larger refractive indices. Thus, particles with larger diameters and/or higher refractive indices are rejected by the OPTIC device. In contrast, particles with smaller diameters and/or lower refractive indices are propelled through the central nanopore and leave the system from the outlet port. This mechanism provides a complete separation capability for smaller nanoparticles (e.g. exosomes) in a heterogeneous mixture through negative depletion. Clogging of the central aperture is prevented by the microlens itself since it keeps the larger particles away from the surface.

Optical radiation force acting on nano-bioparticles can be divided into scattering \mathbf{F}_s and gradient \mathbf{F}_g components, as discussed above, which act along and perpendicular to the optical axis, respectively. While \mathbf{F}_s acts against \mathbf{F}_d , \mathbf{F}_g is directed towards the optical axis. Their magnitudes are given by [14]:

$$F_{s,g} = \frac{2n_m P}{c} Q_{s,g} \quad (1)$$

where P is incident light power, n_m is surrounding medium's refractive index, c is the speed of light and $Q_{s,g}$ is a respective dimensionless parameter representing optical pressure transfer efficiency due to reflection/refraction at material interfaces. It can be analytically calculated for simple beam profiles such as lightly focused Gaussian beams acting on a spherical particle. On the other hand, scenarios that use complex beam profiles or target smaller particles with diameters comparable to the optical wavelength (e.g. $d \sim 1 \mu\text{m}$), the ray optics approximation cannot be used. Instead, a Maxwell stress tensor (MST) approach should be adopted [24, 25].

$$T_{ij} = \epsilon E_i E_j^* + \mu H_i H_j^* - \frac{1}{2} \delta_{ij} (\epsilon |\mathbf{E}|^2 + \mu |\mathbf{H}|^2) \quad (2)$$

where \mathbf{E} and \mathbf{H} are electric and magnetic field vectors, ϵ and μ are the electric permittivity and magnetic permeability of the medium, whereas δ_{ij} is the Kronecker delta symbol. Using MST, the net optical radiation force on a small particle in an arbitrary field profile can be calculated through assuming a bounding box small enough to confine the particle as in [25].

$$F = \oint_S \sum_j \frac{1}{2} \text{Re} (T_{ij} \hat{n}_j) \quad (3)$$

with S being box surface where \hat{n}_j is a unit vector along one of the principal axes.

3. Focusing efficiency of OPTIC microlens

The central nanopore opening plays a key role in precise alignment of fluidic flow along the optical axis and determining the threshold rejection diameter. On the

electromagnetic part, it also controls the focusing characteristics of the OPTIC microlens. Hence, it should be ensured that the focusing behavior does not deteriorate for an admissible d_c range [13]. Focusing patterns of the microlens illuminated by plane waves with $\lambda = 655$ nm for various d_c values are given in **Figure 2a**.

Compared with the cases of no central nanopore (i.e., $d_c = 0$ nm) and a uniform NHA (where $d_c = 150$ nm), the enlarged aperture ($d_c = 500$ nm) has a negligible effect on light focusing behavior, i.e., maximum intensity ($|E|^2$), spot size and depth of field (DoF). Moreover, focusing behavior does not significantly degrade for a large d_c of 800 nm, as seen on the rightmost panel of **Figure 2a**.

The dashed horizontal lines in **Figure 2a**, corresponding to focal point, indicate that the focal length (f_D) is minimally affected by the change of d_c , where it is $5.32 \mu\text{m}$ for d_c up to 500 nm, and slightly increases to $5.56 \mu\text{m}$ for $d_c = 800$ nm. Intensity profiles along the focal axis (i.e., $z = f_D$, dashed lines in **Figure 2a**) are presented in **Figure 2b**. It is clearly seen that the OPTIC microlens brings incident light to a tight focal spot with a full width at half maximum (FWHM) of $1.12 \mu\text{m}$ for $d_c \leq 150$ nm, whereas FWHM tends to slightly increase for $d_c \geq 500$ nm, as it becomes $1.24 \mu\text{m}$ and $1.80 \mu\text{m}$ for $d_c = 500$ nm and 800 nm, respectively. Thus, the focusing characteristics of the microlens is remarkably stable for a broad range of d_c . Variation of optical intensity along the optical axis (z -direction) for different d_c is shown in **Figure 2c**, where almost identical behavior is observed for relatively small size central nanopores ($d_c \leq 150$ nm). DoF also shows little variation for d_c up to 500 nm. Only, a slight increase in focal distance is observed when $d_c = 800$ nm.

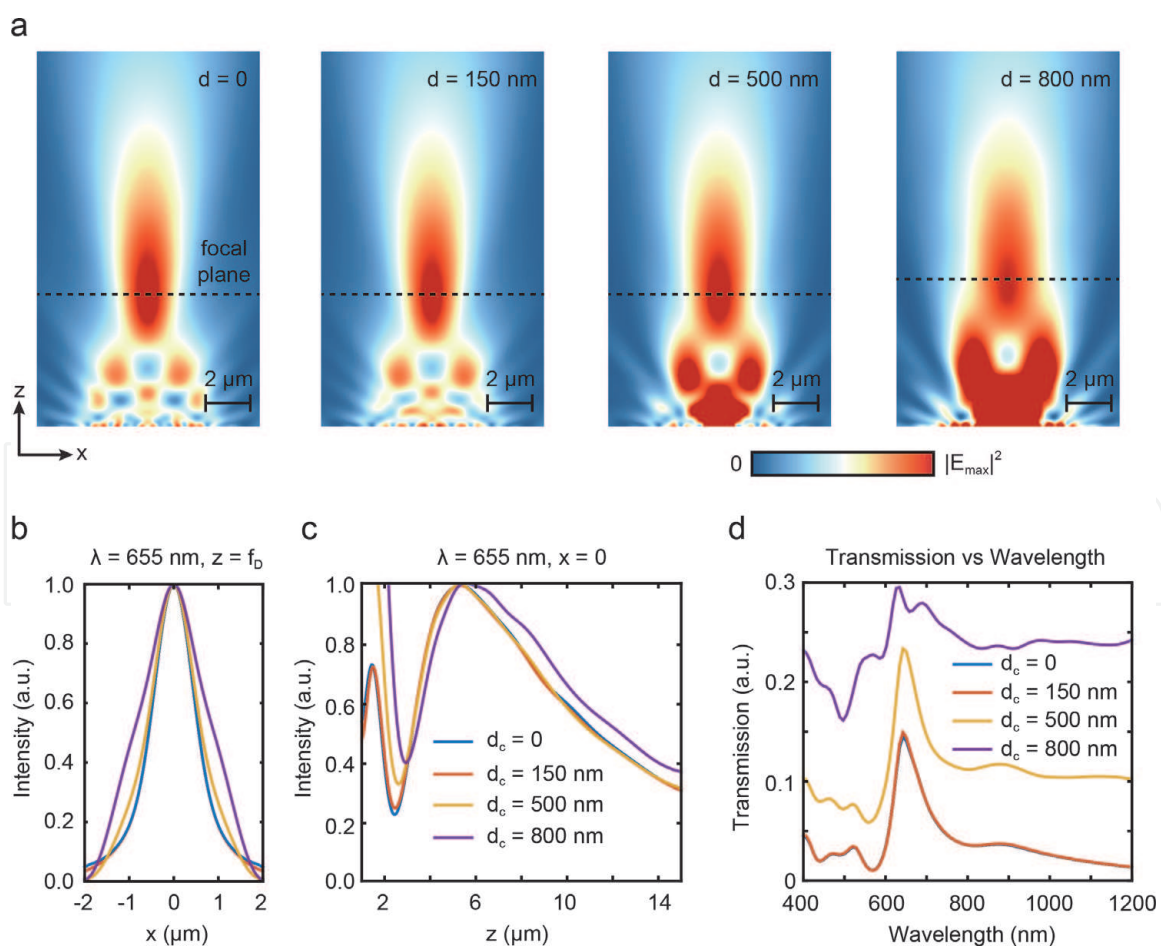


Figure 2. Monochromatic light focusing behavior with varying central nanopore dimensions: (a) focusing behavior of OPTIC microlens for $\lambda = 655$ nm as a function of d_c , corresponding field profile (b) along the focal axis (horizontal dashed lines in (a)) and (c) optical axis. (d) Transmission spectra for plasmonic nanopore devices with different diameter central nanopore openings. Copyright 2020 nature publishing group adapted with permission [11].

The light focusing mechanism of OPtIC microlens relies on the periodic arrangement of smaller nanoholes around the central one. The EOT effect occurs when the Bragg condition is met, i.e., $\mathbf{G} = i\mathbf{G}_x + j\mathbf{G}_y$, where i and j are the corresponding (i, j) grating orders [16, 18]. The transmission spectra shown in **Figure 2d** is obtained using E -field monitors on the focusing side of the microlens. EOT resonance occurs at $\lambda = 650$ nm (55 nm FWHM) for the (1,0) grating coupled condition. This confirms that the light focusing behavior is due to interference of in-phase wave components emanating from the periodic NHA [13]. For the NHA with a large central nanopore ($d_c = 500$ nm), deviation of the EOT peak compared to the NHA without a central opening ($d_c = 0$ nm) is relatively small, although a larger background transmission is observed. However, further increase in the central nanopore dimensions ($d_c = 800$ nm) leads to non-resonant light transmission, manifesting itself as enhanced background signal, as shown in **Figure 2d** (top curve). In the light of the above discussion regarding the fluidic flow around the focal point (see **Figure 1**) and light focusing behavior of NHA, an OPtIC microlens with 9×9 NHA of $d = 150$ nm and $a = 380$ nm, along with a central nanopore opening of $d_c = 500$ nm is adopted for label-free sorting of nano-bioparticles.

An important observation in **Figure 2a** is the checkerboard-like pattern just above the OPtIC microlens surface, which arises from plasmonic Talbot effect, that is diffractive self-imaging of smaller-diameter nanoholes [13, 26]. On the other hand, intensity right over the central aperture is significantly enhanced for $d_c \geq 500$ nm due to diffractive light transmission through it. These two effects are compared in **Figure 3** using near field phase maps where each small nanohole transmits waves with almost identical amplitude and phase, giving rise to in-phase interference around the focal point. Closer inspection of **Figure 3** reveals that the checkerboard pattern is not disrupted when the central aperture is absent (**Figure 3a**) or is larger than the surrounding nanoholes in the array (**Figure 3c**).

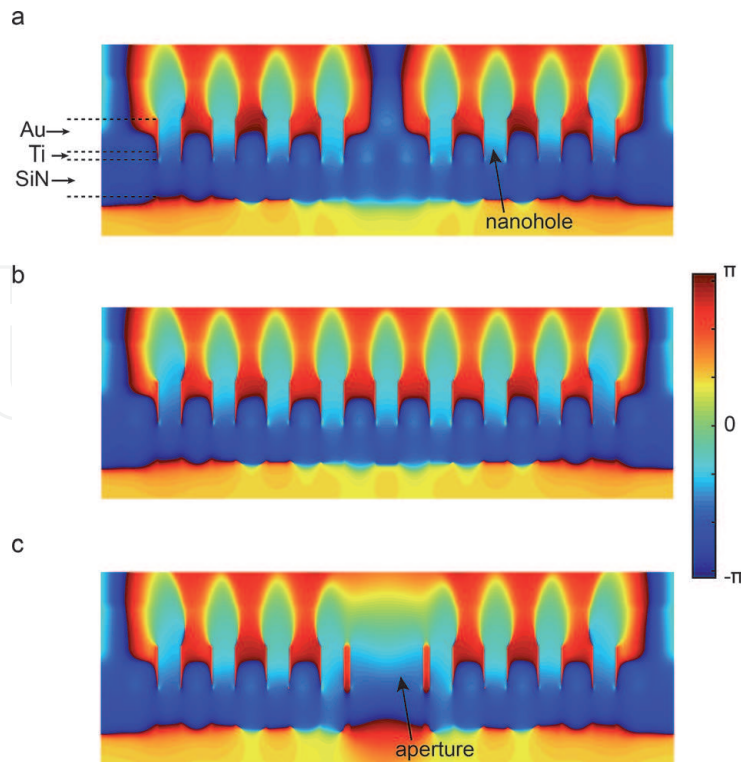


Figure 3. Light focusing behavior due to in-phase interactions: Near-field phase maps of the hot intensity spots around the OPtIC nanopore device are presented for varying d_c when illuminated by a monochromatic plane wave ($\lambda = 655$ nm). d_c is equal to (a) 0 nm (no central nanopore), (b) 150 nm (identical central opening with the NHA pattern) and (c) 500 nm (enlarged central nanopore). Copyright 2020 nature publishing group adapted with permission [11].

Light intensity around the central nanopore opening increases with increasing d_c , as seen in **Figure 2a**. This observation is confirmed in **Figure 2c** where a secondary peak in light intensity close to the microlens surface appears. This peak is less intense than the peak around the focal point for smaller size central nanopores ($d_c \leq 150$ nm). However, it is significantly enhanced for larger size nanopore ($d_c \geq 500$ nm). The high intensity region around the nanopore opening may lead to increased optical scattering force F_s , causing undesired rejection of smaller/lower-refractive index particles that managed to pass the focal region and carried towards the central nanopore. However, in addition to tailoring the central nanopore dimension, one can also take advantage of Stokes flow [1, 9, 11], where the fluidic drag forces scale with the relative velocity of nano-bioparticles (\mathbf{u}) with respect to the flow rate (\mathbf{v}) of medium (i.e., $F_d \propto |\mathbf{u}-\mathbf{v}|$). As fluidic velocity \mathbf{v} is approximately three orders of magnitude higher close to the central nanopore opening with respect to that of the focal point (**Figure 1b**), fluidic drag forces F_d are significantly larger too. Hence, optical scattering force F_s around the nanopore region cannot repel particles that were below the critical diameters. As a result, in the following sections, interplay of forces only around the focal point is considered in the assessment of sorting efficiencies of the OPTIC microlens.

4. Broadband operation of OPTIC microlens

In the preceding section, we showed that the OPTIC nanopore device can focus collimated monochromatic light at $\lambda = 655$ nm (close to the EOT resonance peak) into a tight spot. However, broad spectrum operation is also desirable to utilize low-cost broadband incoherent light sources, such as light emitting diodes (LEDs) and halogen bulbs. Hence, development of microlenses that exhibit minimal chromatic aberration is critical [13]. Here, we examine the broadband light focusing behavior of the OPTIC nanopore device with $d_c = 500$ nm over a wavelength range spanning from 600 nm to 780 nm. **Figure 4a** shows that f_D decreases monotonically with increasing λ with a maximum deviation (Δz_{\max}) that is below 200 nm ($\sim \lambda/33$) between 620 nm and 680 nm, which resides within the FWHM of the EOT peak (**Figure 2d**). Below the short-wavelength tail of the EOT peak, Wood's anomaly [19, 27] leads to longer f_D for $\lambda = 600$ nm at the transmission minimum (**Figure 2d**).

Optical intensity variation along the focal plane (dashed lines in **Figure 4a**) is shown in **Figure 4b**. Focal point has a FWHM of 1.08 μm , 1.12 μm , 1.24 μm and 1.28 μm at $\lambda = 620$ nm, 633 nm, 655 nm and 680 nm, respectively. In addition, the DoF calculated from **Figure 4c** shows small variations within the same spectral window ($620 \text{ nm} < \lambda < 680 \text{ nm}$). However, the DoF is considerably larger at the wavelength of 600 nm that resides outside the EOT spectral window. Therefore, light focusing characteristics over a sufficiently broad range of wavelengths hinges on the (1,0) resonance transmission (EOT) peak.

Using the Rayleigh-Sommerfeld (R-S) formula [13, 28, 29], the focal length of the finite-size NHA microlens can be calculated:

$$\frac{dI}{dz} = -2I_0 \frac{\pi\rho^2}{\lambda z^2} \sin\left(\frac{\pi\rho^2 n}{\lambda z}\right) = 0 \quad (4)$$

where I and I_0 are the intensity values calculated at a distance above the lens along the optical (z) axis and the peak intensity, respectively. Here, ρ is the aperture radius and n is the refractive index of the surrounding medium. Comparison of the solid black curve obtained from FDTD simulations to the gray dots calculated via the R-S formula Eq. (4) are in very good agreement for λ between 620 nm and

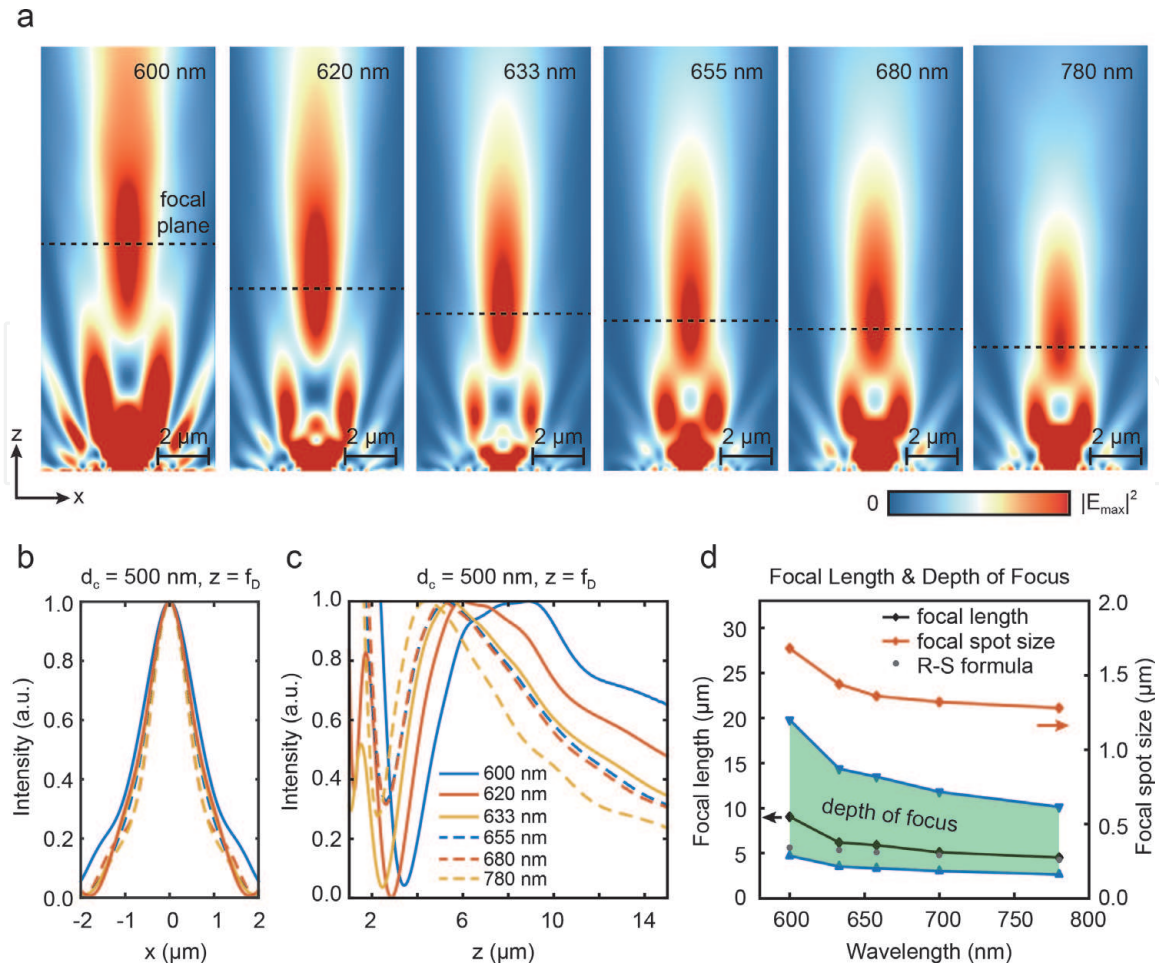


Figure 4. Broadband light focusing: (a) simulated light focusing behavior of the optimized OPTIC microlens with $d_c = 500$ nm for a range of λ , cross-sectional intensity variation along (b) the focal and (c) optical axis, as well as (d) variation of focusing characteristics in terms of f_D , spot size and DoF with λ . the gray dots represent values obtained using the Rayleigh-Sommerfeld formula. Copyright 2020 nature publishing group adapted with permission [11].

680 nm, as seen in **Figure 4d**. The shaded area bounded by the solid blue lines in **Figure 4d** indicates that DoF does not change significantly within the same wavelength range, even though incorporation of an enlarged central aperture breaks the NHA periodicity. Minimal modulation in the focal length and spot size is also shown in **Figure 4d** (the solid black and orange curves, respectively). Thus, the OPTIC microlens exhibits minimal chromatic aberration within the FWHM spread of the EOT peak, offering a well-defined broadband light focusing characteristic.

5. Influence of thermo-plasmonic forces

As conventional wisdom suggests, surface plasmon generation is accompanied by electromagnetic heating, which evokes heat-induced fluid dynamics. The local temperature elevation in the vicinity of the OPTIC microlens induces a buoyance-driven convective fluid flow (Archimedes force) against the reverse main flow stream, resulting in a thermo-plasmonic drag force that drives particles away from the microlens surface [30, 31]. A comprehensive review of this physical mechanism – thermo-induced fluid motion - can be found elsewhere [32, 33]. In this work, thermo-plasmonic drag forces are calculated using Multiphysics FEM simulations, which incorporate electromagnetic (EM) wave, heat transfer and Navier–Stokes equations. Here, we solve the EM wave Equation [34].

$$\nabla \times (\nabla \times \mathbf{E}) - k_0^2 \epsilon(\mathbf{r}) \mathbf{E} = 0 \quad (5)$$

where $k_0 = 2\pi/\lambda_0$ is free-space wavelength and $\epsilon(\mathbf{r})$ is spatial distribution of ϵ at λ_0 . The calculated \mathbf{E} -field is used to find the heat source density $q(\mathbf{r}) = 0.5\text{Re}[\mathbf{J} \cdot \mathbf{E}^*]$, which is employed to find the total heat power using $Q = \int q(\mathbf{r}) dv$, \mathbf{J} being the induced current density in metal [34]. Solving the heat transfer equation simultaneously with the incompressible Navier–Stokes relations,

$$\nabla \cdot [\rho c_p T(\mathbf{r}) \mathbf{v}(\mathbf{r}) - \kappa \nabla T(\mathbf{r})] = Q(\mathbf{r}) \quad (6)$$

$$\rho_0 [\mathbf{v}(\mathbf{r}) \cdot \nabla] \mathbf{v}(\mathbf{r}) + \nabla p(\mathbf{r}) - \eta \nabla^2 \mathbf{v}(\mathbf{r}) = \mathbf{F} \quad (7)$$

where ρ , K , c_p and η are the density, thermal conductivity, constant pressure specific heat capacity and dynamic viscosity of the fluidic medium, respectively. $T(\mathbf{r})$ and $\mathbf{v}(\mathbf{r})$ are the temperature and the fluidic velocity where $\nabla \cdot \mathbf{v} = 0$. Calculations are performed using material parameters that are adopted from the work of Roxworthy et al. [33]. Provided that the EM induced temperature gradient and convective fluid flow distribution are obtained through Eqs. (5)–(7), the volumetric thermo-plasmonic force \mathbf{F}_{tp} and \mathbf{F}_{d} can be calculated through the Boussinesq approximation [31, 33, 35].

$$\mathbf{F}_{\text{tp}} = g \rho_0 \beta(T) [T(\mathbf{r}) - T_0] \hat{\mathbf{z}} \quad (8)$$

and Stoke's equation

$$\mathbf{F}_{\text{d}} = -6\pi\eta r \mathbf{v} \quad (9)$$

where g denotes the gravitational acceleration constant and β is the thermal expansion coefficient of the water.

Steady-state 2D temperature spatial distributions in the x - y (**Figure 5a**) and x - z planes (**Figure 5b**) are calculated using Eqs. (5)–(9). To demonstrate the dynamical

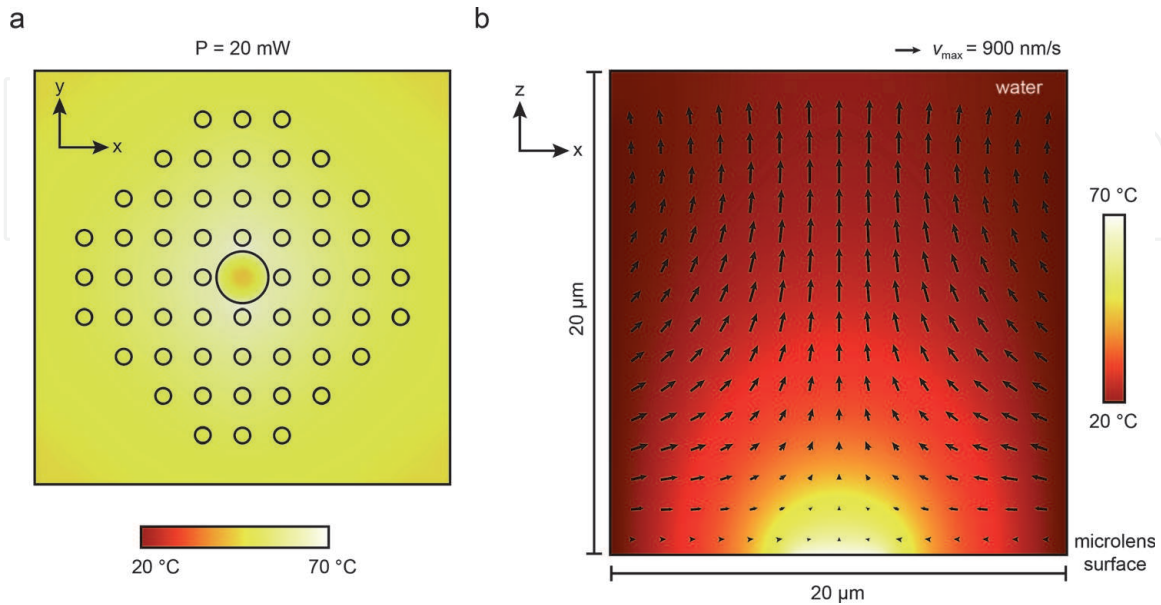


Figure 5. Thermo-plasmonic heating and Rayleigh–Bénard flow: (a) temperature distribution on the OPTIC nanopore device surface under illumination (633 nm wavelength and 20 mW total power). (b) Temperature distribution and heat-induced fluidic flow pattern on a perpendicular plane crossing the optical axis. The arrows represent the velocity vector \mathbf{v} . copyright 2020 nature publishing group adapted with permission [11].

properties of the thermal-induced fluid convection, the temperature distribution is deliberately overlaid on a vertical 2D slice of convection velocity profile within the same x - z plane (**Figure 5b**). In our FEM simulations, the wavelength and power of the excitation light beam is assumed to be 633 nm and 20 mW, respectively. The ambient temperature is $T_0 = 20$ °C. The ambient temperature near and across the microlens surface is considerably increased due to endogenous heat generation via dissipative losses. Because light transmitting through the central aperture is mostly diffractive in nature and lightly coupled to the surface plasmon polariton (SPP) modes of the NHA, a relatively small temperature increase takes place close to the enlarged aperture region. On the contrary, a significant amount of heat is generated outside the central aperture area, which is attributed to non-radiative damping of SPPs launched on the metal/dielectric interface. Due to the large differences in the heat conductivity of Au and water, heat dissipation occurs slowly along the optical axis of the microlens within the solution environment. This results in reduction of the mass density of ambient water, leading to an upward-directed convective fluidic flow that possesses the features of a toroidal Rayleigh–Bénard flow [33], as represented by the arrows in **Figure 5b**. Here, \mathbf{v} is along the optical axis in the $+z$ direction, exerting a drag force on the suspended nano-bioparticles that directs them away from the microlens surface. Our calculations show that the maximum heat induced convective flow velocity is $v_{\max} = 900$ nm/s, whereas the flow velocity is $v = 360$ nm/s at the focal point.

6. Label-free sorting of nano-bioparticles

OPtIC nanopore device enables both size- and refractive-index based separation of nano-bioparticles by utilizing a delicate balance of counteracting forces, i.e., \mathbf{F}_s , \mathbf{F}_d , \mathbf{F}_{tp} and \mathbf{W} (gravitational force). Since these forces act along the optical axis within the focal point region, selective particle elution can be readily achieved by adjusting the net force $\mathbf{F}_{\text{net}} = \mathbf{F}_s + \mathbf{F}_d + \mathbf{F}_{\text{tp}} + \mathbf{W}$ [11]. We calculated \mathbf{F}_{net} for varying spherical bioparticles with a mass density of 1.05 g/cm³ and refractive index of 1.55. The direction of \mathbf{F}_{net} as a function of distance from the microlens ($0 \leq z \leq 6$ μm) and particle diameter (100 nm $\leq d \leq 1.0$ μm) is shown in **Figure 6a** and **b**. In both cases, incident light power is 20 mW and wavelength 633 nm, and the fluidic flow velocities at the focal point $v(z = f_D)$ are 1.3 $\mu\text{m/s}$ and 3.0 $\mu\text{m/s}$. The red and blue shaded regions in **Figure 6a** and **b** correspond to the positive ($F_s + F_{\text{tp}} > F_d + W$, blue shaded region) and negative ($F_s + F_{\text{tp}} < F_d + W$, red shaded region) net forces, respectively.

F_{net} is always negative for $d \leq 200$ nm, as indicated by the white dashed line on the left in **Figure 6a**. Nano-bioparticles smaller than this threshold diameter, $d < d_{th} = 200$ nm can travel a path along the optical axis and pass through the nanopore opening towards the outlet port. Particles with diameters larger than d_{th} experience stronger optical scattering and thermo-plasmonic drag forces ($F_s + F_{\text{tp}}$) relative to the fluidic drag and gravitational forces ($F_d + W$). Therefore, they are retained in the top chamber. Hence, under the above-stated flow and illumination conditions, small particles ($d \leq 200$ nm) get separated from relatively large bioparticles. The OPtIC nanopore device offers selective particle fractionation by adjusting either the incident light power or bulk fluidic flow rate. At a fixed incident light power of 20 mW, when $v(z = f_D)$ is increased to 3.0 $\mu\text{m/s}$, the threshold particle diameter d_{th} is shifted to 350 nm (**Figure 6b**). By further tuning, relative contributions of acting forces can be tailored for selective separation of nano-bioparticles with diameters up to 500 nm, as larger particles cannot physically pass through the nanopore opening ($d_c = 500$ nm).

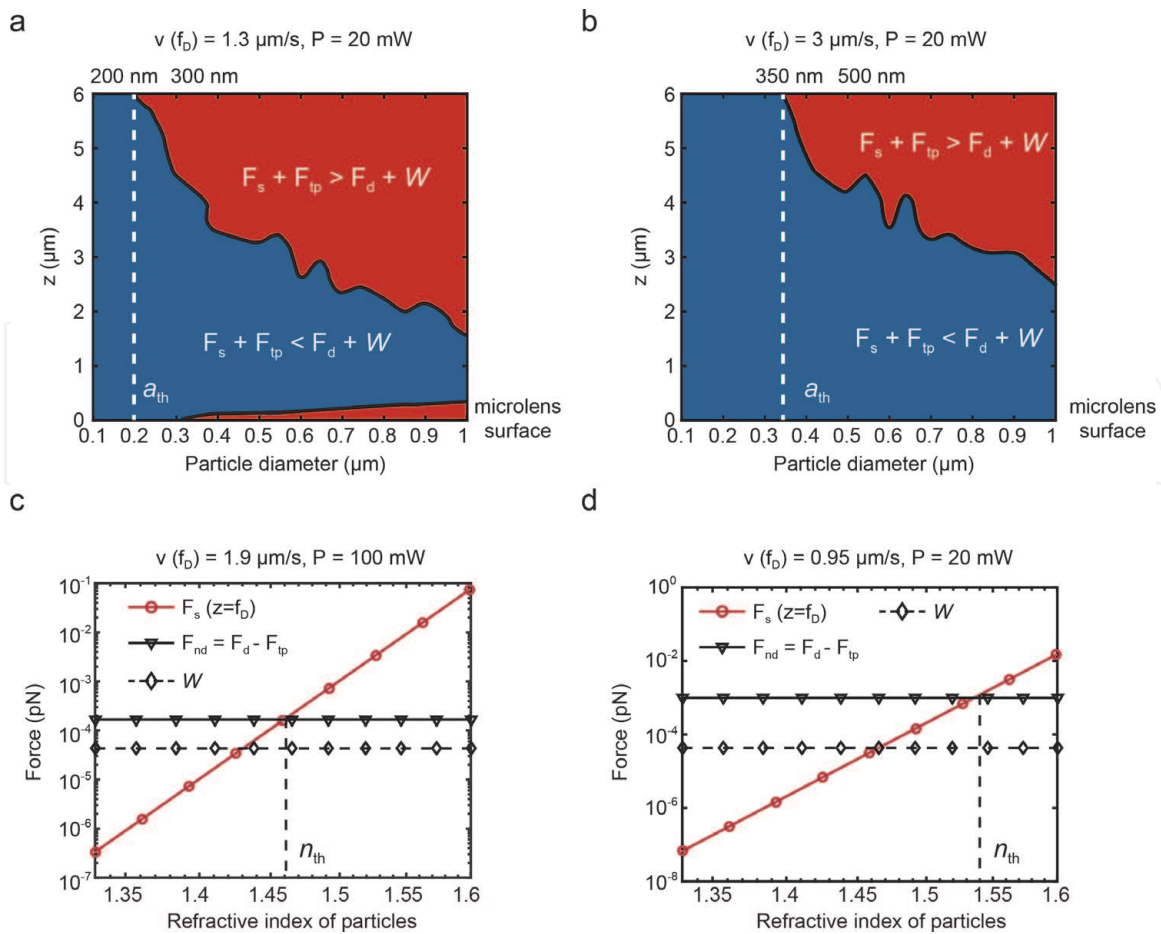


Figure 6. Label-free selective sorting of nanoparticles: F_{net} as a function of particle diameter and position along the optical axis is shown for a fluidic flow rate of (a) $1.3 \mu\text{m/s}$ and (b) $3.0 \mu\text{m/s}$ at the focal point $v(z = f_D)$. A monochromatic light source (633 nm) with 20 mW power is assumed. (c) Forces acting on a fixed diameter ($d = 200 \text{ nm}$) nanoparticle at the focal point as a function of particle refractive index (n_e) is shown for a fluidic flow velocity of (c) $v(z = f_D) = 1.9 \mu\text{m/s}$ under 100 mW illumination. (d) Calculations are repeated for a fluidic flow velocity of $v(z = f_D) = 0.95 \mu\text{m/s}$ under 20 mW illumination. The dashed vertical lines in (a) and (b) represent threshold particle diameters, while those in (c) and (d) denote threshold particle refractive indices n_e . The lines in (c) and (d) are first-order polynomial fits to the numerical data. Copyright 2020 nature publishing group adapted with permission [11].

Size-based separation is not adequate when similar size bioparticles of different origins need to be separated. As indicated in Eq. (1), the optical radiation force acting on particles is a function of both particle radius and refractive index. In this respect, particles comparable dimensions can be separated based on their refractive indices [4, 7]. In general, refractive index is intimately linked to the internal structure and chemical makeup of the nano-bioparticles [e.g., exosomes, viruses]. A recent research study has shown that implementation of optical chromatography based on refractive index differences yield successful differentiation of cells with single gene modifications [3]. We calculated forces (F_s , F_{tp} , F_d , W) acting on the nanoparticles ($d = 200 \text{ nm}$) as a function of refractive index ($1.33 < n_e < 1.6$) at the focal point ($z = f_D = 5.32 \mu\text{m}$). A fluidic flow rate of $v(f_D) = 1.9 \mu\text{m/s}$ and 100 mW monochromatic light illumination at 633 nm is assumed. Solid red and black curves in **Figure 6c** depicts optical scattering F_s and the net drag (i.e., $F_{nd} = F_d - F_{tp}$) forces, respectively. The dashed curves represent contribution of the gravitational force (W). In our calculations, n_e is varied from $n_{\text{water}} = 1.33$ to $n_{\text{ps}} = 1.6$ (polystyrene beads). As depicted in **Figure 6c**, at the flow rate ($1.9 \mu\text{m/s}$), the magnitude of F_s increases with n_e and F_s balances F_{nd} when $n_e = 1.46$ (indicated by the vertical dashed line). For smaller n_e , drag force originating from the primary fluidic flow dominates the opposing forces ($F_s + F_{tp}$). Thus, the OPTIC microlens can be

employed for selective separation of nano-bioparticles with a threshold of $n_e = 1.46$, corresponding to the refractive index of phospholipids and proteins.

It is known that exosomes (nanovesicles composed mostly of water enclosed by a thin phospholipid membrane) have lower refractive indices n_e in the range of 1.37–1.39 [36–38], which is closer to $n_e = 1.33$ of water. In contrast, virions are tight assemblies of nucleic acids, proteins and lipids with higher n_e around 1.48 [39]. For an exosome-like bioparticle ($d = 200$ nm) with $n_e \sim 1.38$, F_s can be as small as 4 aN, which is two orders of magnitude smaller than the corresponding value for $n_e = 1.48$ (~ 400 aN) for a similar size virion. Hence, our OPtIC nanopore device can selectively separate exosomes from similar size virions with high efficiencies.

The threshold n_e can be readily tuned, as in the case of particles size, by adjusting the fluidic flow velocity and/or light power. **Figure 6d** shows that the threshold refractive index can be tuned to $n_e = 1.54$ when the fluidic flow rate is halved to 0.95 $\mu\text{m/s}$ and light power is reduced to 20 mW. Since OPtIC nanopore devices can be operated by directly incident light using an objective-free focusing mechanism, a number of them can be implemented on a planar chip. One can combine multiple OPtIC devices to achieve multi-stage sequential fractionation of nano-bioparticles to realize highly specific size and refractive index-based separation.

7. Radial lining-up of nano-bioparticles

A major limitation of conventional OC is the difficulty of aligning fluidic flow against a lightly focused Gaussian beam in a precise manner [6]. Our OPtIC nanopore device employs a self-collimation mechanism effortlessly aligning fluidic flow along the optical axis of the microlens. This self-collimation capability, lining-up particles against the scattering force, is demonstrated in **Figure 7**. We calculated radial components of the optical gradient (F_{g-r}), fluidic drag (F_{d-r}) and thermo-plasmonic (F_{tp-r}) forces at the focal point $z = f_D$. We analyzed 200 nm (**Figure 7a**) and 600 nm (**Figure 7b**) diameter particles, assuming a fluidic flow velocity of v ($z = f_D$) = 1.3 $\mu\text{m/s}$ at the focal point and a 20 mW monochromatic (633 nm wavelength) light source. As shown in **Figure 7a**, these radial forces act like a

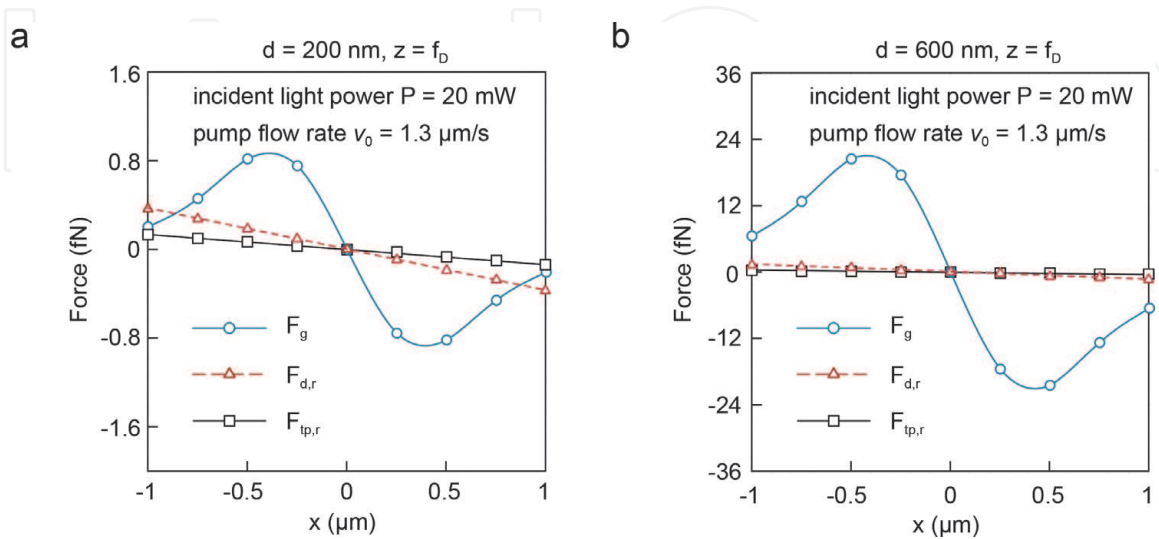


Figure 7.

Self-collimating radial forces along the optical axis: The radial components of F_g , F_d and F_{tp} in the direction perpendicular to the optical axis is shown for (a) 200 nm and (b) 600 nm particles. The operation conditions are 20 mW light power at 633 nm and a fluidic flow velocity 1.3 $\mu\text{m/s}$ at the focal point. Copyright 2020 nature publishing group adapted with permission [11].

restoring mechanism ($F \propto -x$) within $\pm 1 \mu\text{m}$ away from the optical axis. Nano-bioparticles that deviate from the optical axis are pushed back towards it ($x = 0$) by these radial restoring forces. This leads to minimal spatial dispersion of the nano-bioparticles in the radial direction. As shown in **Figure 7b**, larger particles ($d = 600 \text{ nm}$) experience at least an order of magnitude larger optical gradient forces. This enables precise alignment of larger particles against the optical scattering force at the focal point, a critical requirement for selective rejection of particles above a threshold diameter.

As shown in **Figure 7**, nanoparticles in the focal are mainly retained along the optical axis by the optical gradient force F_{g-r} , which is significantly stronger than F_{d-r} . Optical gradient force F_{g-r} is relatively stable and readily tuned using light intensity. Hence, self-collimation mechanism employed by our OPTIC nanopore device is robust against fluctuations in the fluidic flow rate.

8. Conclusion

In this chapter, we reviewed a facile optofluidic nanopore platform for the purposes of optical chromatography of nano-bioparticles based on their size and/or refractive index (chemical composition). Consisting of a finite-size periodic plasmonic nanohole array on a suspended membrane, this OPTIC nanopore device with an enlarged central aperture facilitates precise alignment of optical scattering, thermo-plasmonic drag, and fluidic drag forces against each other for the purposes of OC. Its self-collimation mechanism eliminates the need for sophisticated and bulky optic components (e.g., lasers, microscope objectives, multi-axis stages, etc.) that are commonly used in conventional OC techniques. Furthermore, our plasmonic microlens opens the door to use of incoherent light source, such as LEDs, for the purposes of OC by readily focusing collimated broadband light into a tight spot. This lensing mechanism provides a robust separation capability that is insensitive to structural variations of the central nanopore. We demonstrated size-based selective sorting of nano-bioparticles, such as exosomes, with a tunable threshold diameter using incident light power or fluidic flow rate. In addition, refractive-index based separation of identical size nano-bioparticles are shown. Similar to size-based separation, the refractive-index (material composition) based separation mechanism is readily tunable through incident light power and fluidic flow rate.

Acknowledgements

A. A. Yanik acknowledges support from National Science Foundation [ECCS-1611290], Gordon and Betty Moore Foundation [GBMF #5263.06], and National Science Foundation CAREER Award [ECCS-1847733]. X. Zhu was supported by a University of California Chancellor's Dissertation Year Fellowship. We acknowledge Dr. Tom Yuzvinsky for assistance with device fabrication and the W.M. Keck Center for Nanoscale Optofluidics for use of the FEI Quanta 3D.

Conflict of interest

The authors declare no conflict of interest.

IntechOpen

Author details

Xiangchao Zhu¹, Ahmet Cicek², Yixiang Li¹ and Ahmet Ali Yanik^{1,3*}

¹ Department of Electrical Engineering, Jack Baskin School of Engineering, University of California Santa Cruz, Santa Cruz, CA, USA

² Department of Nanoscience and Nanotechnology, Faculty of Arts and Science, Burdur Mehmet Akif Ersoy University, Burdur, Turkey

³ California Institute for Quantitative Biosciences (QB3), University of California Santa Cruz, Santa Cruz, CA, USA

*Address all correspondence to: yanik@ucsc.edu

IntechOpen

© 2021 The Author(s). Licensee IntechOpen. This chapter is distributed under the terms of the Creative Commons Attribution License (<http://creativecommons.org/licenses/by/3.0>), which permits unrestricted use, distribution, and reproduction in any medium, provided the original work is properly cited. 

References

- [1] Imasaka T, Kawabata Y, Kaneta T, Ishidzu Y. Optical chromatography. *Analytical Chemistry*. 1995;67:1763–1765. DOI: 10.1021/ac00107a003
- [2] Hebert CG, Terray A, Hart SJ. Toward Label-Free Optical Fractionation of Blood-Optical Force Measurements of Blood Cells. *Analytical Chemistry*. 2011;83: 5666–5672. DOI: 10.1021/ac200834u
- [3] Ma Z, Burg KJL, Wei Y, Yuan X-C, Peng X, Gao BZ. Laser-guidance based detection of cells with single-gene modification. *Applied Physics Letters*. 2008;92:213902. DOI: 10.1063/1.2938020
- [4] Hart SJ, Terray A, Leski TA, Arnold J, Stroud R. Discovery of a Significant Optical Chromatographic Difference between Spores of *Bacillus anthracis* and Its Close Relative, *Bacillus thuringiensis*. *Analytical Chemistry*. 2006;78:3221–3225. DOI: 10.1021/ac052221z
- [5] Kaneta T, Ishidzu Y, Mishima N, Imasaka T. Theory of optical chromatography. *Analytical Chemistry*. 1997;69:2701–2710. DOI: 10.1021/ac970079z
- [6] Makihara J, Kaneta T, Imasaka T. Optical chromatography: Size determination by eluting particles. *Talanta*. 1999;48:551–557. DOI: 10.1016/S0039-9140(98)00272-0
- [7] Hart SJ, Terray AV. Refractive-index-driven separation of colloidal polymer particles using optical chromatography. *Applied Physics Letters*. 2003;83:5316–5318. DOI: 10.1063/1.1635984
- [8] Taylor JD, Terray A, Hart SJ. Analytical particle measurements in an optical microflume. *Analytica Chimica Acta*. 2010;670:78–83. DOI: 10.1016/j.aca.2010.04.062
- [9] Terray A, Hebert CG, Hart SJ. Optical chromatographic sample separation of hydrodynamically focused mixtures. *Biomicrofluidics*. 2014;8: 064102. DOI: 10.1063/1.4901824
- [10] Terray A, Taylor JD, Hart SJ. Cascade optical chromatography for sample fractionation. *Biomicrofluidics*. 2009;3:044106. DOI: 10.1063/1.3262415
- [11] Zhu X, Cicek A, Li Y, Yanik AA. Plasmo-fluidic microlenses for label-free optical sorting of exosomes. *Sci Rep*. 2019;9:8593. DOI:10.1038/s41598-019-44801-3
- [12] Verslegers L, Catrysse PB, Yu Z, White JS, Barnard ES, Brongersma ML, Fan S. Planar lenses based on nanoscale slit arrays in a metallic film. *Nano Letters*. 2008;9:235–238. DOI: 10.1021/nl802830y
- [13] Gao H, Hyun JK, Lee MH, Yang JC, Lauhon LJ, Odom TW. Broadband plasmonic microlenses based on patches of nanoholes. *Nano Letters*. 2011;10: 4111–4116. DOI: 10.1021/nl1022892
- [14] Ashkin A. Acceleration and trapping of particles by radiation pressure. *Physical Review Letters*. 1970;24:156–159. DOI: 10.1103/PhysRevLett.24.156
- [15] Ashkin A, Dziedzic J. Optical trapping and manipulation of viruses and bacteria. *Science*. 1987;235:1517–1520. DOI: 10.1126/science.3547653
- [16] Ebbesen TW, Lezec HJ, Ghaemi HF, Thio T, Wolff PA. Extraordinary optical transmission through sub-wavelength hole arrays. *Nature*. 1998;391:667–669. DOI: 10.1038/35570
- [17] Martin-Moreno L, Garcia-Vidal FJ, Lezec HJ, Pellerin KM, Thio T, Pendry JB, Ebbesen TW. Theory of extraordinary optical transmission through subwavelength hole arrays.

- Physical Review Letters. 2001;86:1114–1117. DOI: 10.1103/PhysRevLett.86.1114
- [18] Genet C, Ebbesen TW. Light in tiny holes. *Nature*. 2007;445:39–46. DOI: 10.1038/nature05350
- [19] Yanik AA, Wang X, Erramilli S, Hong MK, Altug H. Extraordinary midinfrared transmission of rectangular coaxial nanoaperture arrays. *Applied Physics Letters*. 2008;93:081104. DOI: 10.1063/1.2973165
- [20] Yanik AA, Huang M, Artar A, Chang T-Y, Altug H. Integrated nanoplasmonic-nanofluidic biosensors with targeted delivery of analytes. *Applied Physics Letters*. 2010;96:021101. DOI: 10.1063/1.3290633
- [21] Huang M, Yanik AA, Chang T-Y, Altug H. Sub-wavelength nanofluidics in photonic crystal sensors. *Optics Express*. 2009;17:24224–24233. DOI: 10.1364/OE.17.024224
- [22] Yanik AA, Cetin AE, Huang M, Artar A, Mousavi SH, Khanikaev A, Connor JH, Shvets G, Altug H. Seeing protein monolayers with naked eye through plasmonic Fano resonances. *Proceedings of the National Academy of Sciences of the United States of America*. 2011;108:11784–11789. DOI: 10.1073/pnas.1101910108
- [23] Oh KW, Lee K, Ahn B, Furlani EP. Design of pressure-driven microfluidic networks using electric circuit analogy. *Lab on a Chip*. 2012;12:515–545. DOI: 10.1039/C2LC20799K
- [24] Okamoto K, Kawata S. Radiation force exerted on subwavelength particles near a nanoaperture. *Physical Review Letters*. 1999; 83:4534–4537. DOI: 10.1103/PhysRevLett.83.4534
- [25] Wang X, Wang X-B, Gascoyne PR. General expressions for dielectrophoretic force and electrorotational torque derived using the Maxwell stress tensor method. *Journal of Electrostatics*. 1997; 39:277–295. DOI: 10.1016/S0304-3886(97)00126-5
- [26] Dennis MR, Zheludev NI, de Abajo FJG. The plasmon Talbot effect. *Optics Express*. 2007;15:9692–9700. DOI: 10.1364/OE.15.009692
- [27] Ghaemi HF, Thio T, Grupp DE, Ebbesen TW, Lezec HJ. Surface plasmons enhance optical transmission through subwavelength holes. *Physical Review B*. 1998;58:6779–6782. DOI: 10.1103/PhysRevB.58.6779
- [28] Ruffieux P, Scharf T, Herzig HP, Völkel R, Weible KJ. On the chromatic aberration of microlenses. *Optics Express*. 2006;14:4687–4694. DOI: 10.1364/OE.14.004687
- [29] Saxena S, Chaudhary RP, Singh A, Awasthi S, Shukla S. Plasmonic Micro Lens for Extraordinary Transmission of Broadband Light. *Scientific Reports* 2014;4:5586. DOI: 10.1038/srep05586
- [30] Baffou G, Girard C, Quidant R. Mapping Heat Origin in Plasmonic Structures. *Physical Review Letters*. 2010;104:136805. DOI: 10.1103/PhysRevLett.104.136805
- [31] Donner JS, Baffou G, McCloskey D, Quidant R. Plasmon-Assisted Optofluidics. *ACS Nano*. 2011;5:5457–5462. DOI: 10.1021/nn200590u
- [32] Kim J. Joining plasmonics with microfluidics: from convenience to inevitability. *Lab on a Chip*. 2012;12: 3611–3623. DOI: 10.1039/C2LC40498B
- [33] Roxworthy BJ, Bhuiya AM, Vanka SP, Toussaint Jr KC. Understanding and controlling plasmon-induced convection. *Nature Communications*. 2014;5:3173, DOI: 10.1038/ncomms4173
- [34] Jackson JD. *Classical Electrodynamics*. 3rd ed. New York:

John Wiley and Sons; 1999. 832 pp.
ISBN: 978-0-471-30932-1

[35] Ndukaife JC, Kildishev AV, Agwu Nnanna AG, Shalaev VM, Wereley ST, Boltasseva A. Long-range and rapid transport of individual nano-objects by a hybrid electrothermoplasmonic nanotweezer. *Nature Nanotechnology*. 2016;11:53–59. DOI:10.1038/nnano.2015.248

[36] van der Pol E, de Rond L, Coumans FAW, Gool EL, Böing AN, Sturk A, Nieuwland R, van Leeuwen TG. Absolute sizing and label-free identification of extracellular vesicles by flow cytometry. *Nanomedicine*. 2018;14:801–810. DOI: 10.1016/j.nano.2017.12.012

[37] van der Pol E, Coumans F, Varga Z, Krumrey M, Nieuwland R. Innovation in detection of microparticles and exosomes. *Journal of Thrombosis and Haemostasis*. 2013;11:36–45. DOI: 10.1111/jth.12254

[38] Gardiner C, Shaw M, Hole P, Smith J, Tannetta D, Redman CW, Sargent IL. Measurement of refractive index by nanoparticle tracking analysis reveals heterogeneity in extracellular vesicles. *Journal of Extracellular Vesicles*. 2014;3:25361, DOI: 10.3402/jev.v3.25361

[39] Wang S, Shan X, Patel U, Huang X, Lu J, Li J, Tao N. Label-free imaging, detection, and mass measurement of single viruses by surface plasmon resonance. *Proceedings of the National Academy of Sciences of the United States of America*. 2010;107:16028–16032. DOI: 10.1073/pnas.1005264107